Three-dimensional Structure of Rhesus Rotavirus by Cryoelectron Microscopy and Image Reconstruction

Mark Yeager,* Kelly A. Dryden,‡ Norman H. Olson,‡ Harry B. Greenberg,§ and Timothy S. Baker‡

*Scripps Clinic and Research Foundation, Department of Molecular Biology, La Jolla, California 92037; ‡Purdue University, Department of Biological Sciences, West Lafayette, Indiana 47907; and §Division of Gastroenterology, Stanford University Medical Center, Stanford, California 94305

Abstract. The structure of rhesus rotavirus was examined by cryoelectron microscopy and image analysis. Three-dimensional reconstructions of infectious virions were computed at 26- and 37-Å resolution from electron micrographs recorded at two different levels of defocus. The major features revealed by the reconstructions are (a) both outer and inner capsids are constructed with $T = 13l$ icosahedral lattice symmetry; (b) 60 spikelike projections, attributed to VP4, extend at least 100 Å from the outer capsid surface; (c) the outer capsid, attributed primarily to VP7, has a smoothly rippled surface at a mean radius of 377 Å and is perforated by 132 aqueous holes ranging from 40–65 Å in diameter; (d) the inner capsid has a "bristled" outer surface composed of 260 trimeric-shaped columns of density, attributed to VP6, which merge with a smooth, spherical shell of density at a lower, mean radius of 299 Å, and which is perforated by holes in register with those in the outer capsid; (e) a "core" region contains a third, nonspherical shell of density at a mean radius of 255 Å that encapsidates the double-stranded RNA genome; and (f) the space between the outer and inner capsids forms an open aqueous network that may provide pathways for the diffusion of ions and small regulatory molecules as well as the extrusion of RNA. The assignment of different viral structural proteins to specific features of the reconstruction has been tentatively made on the basis of excluded volume estimates and previous biochemical characterizations of rotavirus.

ROTAVIRUS is the primary cause of infant gastroenteritis in numerous mammalian and avian species and is the major cause of human infant mortality in developing countries, accounting for the loss of over one million lives each year (Kapikian and Chanock, 1985).

Rotavirus, a member of the *Reoviridae* family, is named on the basis of its double-shelled, spokelike appearance in electron micrographs of negatively stained preparations (hence, the Latin root "rota" meaning "wheel") (Flewett et al., 1974). Virions are commonly described as being composed of two capsid layers inside of which resides a "core" containing the 11 double-stranded RNA genome segments (Estes, Palmer, and Obijeski, 1983). The exact number of structural proteins in mature virions has not been firmly established. However, it is known that four proteins VP2 (94 kD), VP4[1] (88 kD), VP6 (41 kD), and VP7 (34 kD) comprise most of the virion mass (Estes, Palmer, and Obijeski, 1983; Holmes, 1983; Liu, Offit, and Estes, 1988). VP1 (125 kD), VP2, and VP3 (88 kD) are protein components thought to be associated with the virus "core" particle (Palmer, Martin, and Murphy, 1977; Bican et al., 1982; Ludert et al.,

1986; Sandino et al., 1986; Liu, Offit, and Estes, 1988). VP6 is the major inner capsid protein (Kapikian and Chanock, 1985; Gorziglia et al., 1985) and contains the subgroup determinant (Kalica et al., 1981). The major outer capsid protein, VP7, is glycosylated and determines the viral serotype (Bastardo and Holmes, 1980; Kalica et al., 1981). VP4 is also an outer capsid protein and manifests hemagglutinin activity (Kalica, Flores, and Greenberg, 1983). Proteolytic cleavage of VP4 by trypsin generates VP5* and VP8* (López et al., 1985), which remain bound to the virus particle and have a combined molecular mass close to that of VP4. This proteolytic event appears to play a central role both in the enhancement of viral infectivity (Graham and Estes, 1980; Clark et al., 1981; López et al., 1986) and also in the mediation of viral entry into the cell (Fukuhara et al., 1987; Kaljot et al., 1988). In addition, VP4 is known to be a neutralization antigen. Antibodies directed against VP4 mediate both homotypic and heterotypic protection (Offit, Shaw, and Greenberg, 1986; Mackow et al., 1988a). Additional genetic and nucleic acid sequence studies have also contributed evidence for a direct role of VP4 as a determinant of virulence (Flores et al., 1986; Gorziglia et al., 1986; Offit et al., 1986).

A search for suitable methods for treating rotavirus infections has prompted a concerted effort to develop an effective

---

1. The product of gene segment 3 has now been determined to be a structural protein of rotavirus and is referred to as VP3. The gene segment 4 product, previously called VP3, is now named VP4 (Liu, Offit, and Estes, 1988).

vaccine (Midthun et al., 1985). Rhesus rotavirus (RRV)[2] represents an appealing candidate for a live vaccine since it grows in tissue culture to a high titer, is serologically identical to a human rotavirus strain, and is clearly attenuated in man (Hoshino et al., 1984; Flores et al., 1987). In addition, RRV is a useful prototype for structural studies using cryoelectron microscopy since (a) it is readily isolated in a native state whereas human rotavirus is less readily grown; (b) RRV is one of the most extensively studied strains of rotavirus (the amino acid sequences of both RRV coat proteins are known; Mackow et al., 1988a, b); and (c) several monoclonal antibodies have been elicited to different sites in VP5*, VP8*, and VP7 (Mackow et al., 1988a,b). Thus, RRV provides an excellent system for structural labeling studies in which antibody probes might be used to identify specific epitopes on different viral proteins.

Cryoelectron microscopy techniques were used to preserve and examine the "native" structure of RRV without introducing potential artifacts commonly associated with conventional preparation methods involving chemical fixation, dehydration, embedding, shadowing, or staining (Unwin, 1986; Chiu, 1986; Dubochet et al., 1988). Negative staining, for example, typically reveals only those surface features that are accessible to solvent, whereas images of frozen-hydrated specimens also reveal internal structural features. Contrast in unstained, vitrified specimens arises from differences in scattering density among protein, nucleic acid, and solvent components and is also enhanced by judicious defocusing of the electron image (Taylor and Glaeser, 1976; Jaffe and Glaeser, 1984; Milligan, Brisson, and Unwin, 1984).

This report describes the determination of the three-dimensional structure of RRV, obtained by recording transmission electron micrographs of frozen-hydrated specimens and the subsequent combination of several distinct virus particle images using icosahedral image reconstruction techniques. A previous analysis of rotavirus strain SA11 using cryoelectron microscopy revealed virions with a diameter of 765 Å and an icosahedral surface lattice of $T = 13$ (Prasad et al., 1988). The 40-Å resolution map displayed sixty spikes[3] projecting from the smooth outer capsid surface that was penetrated by large aqueous holes. The "bristly" inner capsid surface was also penetrated by holes in radial register with those in the outer capsid. Our analysis reveals that the overall morphologies of strains RRV and SA11 (Prasad et al., 1988, 1990) are quite similar. However, the RRV reconstructions computed at 26-Å resolution reveal additional features about the spike structure and about the organization and morphology of the multishelled virions not reported in lower resolution studies.

Materials and Methods

Virus Samples

RRV was grown in MA104 cells as previously described (Kaljot et al., 1988) except that, after inoculation and a 1-h incubation with trypsin-activated virus, the cells were washed twice and fed with media 199 without

---

2. *Abbreviation used in this paper*: RRV, rhesus rotavirus.

---

3. The 60 features that project above the virion surface are hereafter called "spikes" in accordance with common usage, although it must be stressed that this term grossly oversimplifies the description of a structure with a complex morphology (see Fig. 11).

trypsin. RRV was purified by cesium chloride density gradient centrifugation as described (Shaw et al., 1985).

Cryoelectron Microscopy

Holey triafol films, prepared by the method of Fukami and Adachi (1965), were applied to acetone-cleaned, 400-mesh copper grids. The films were carbon-coated and made hydrophilic by glow discharge in an atmosphere of amylamine. A 5-μl droplet of virus sample ($\sim$5 mg/ml) was allowed to adhere to the support film for $\sim$1 min, followed by blotting with preheated filter paper. Immediately upon removal of the paper, the grid was plunged into an ethane slush and then transferred to liquid nitrogen for indefinite storage.

Grids were transferred from liquid nitrogen to a precooled specimen holder (Gatan, Inc., Warrendale, PA) that maintained the frozen-hydrated sample at -165°C in a Philips EM400T transmission electron microscope operated at 100 kV. Suitable specimen areas were located at low magnification (2,800$\times$) using an electron beam just intense enough ($<0.05 e^-/\text{Å}^2/\text{s}$) so the holes in the support film could be recognized and the relative thickness of the vitrified sample could be estimated. Focusing adjustments and correction for astigmatism were performed at high magnification (170,000$\times$) in an area adjacent to the one photographed. Images were recorded using low-irradiation procedures ($\sim$10 $e^-/\text{Å}^2$) on Kodak SO-163 film at a nominal magnification of 46,000. The two micrographs selected for analysis were recorded at $\sim$3 μm (Fig. 1 a) and $\sim$0.8 μm (Fig. 1 b) underfocus and displayed minimal astigmatism and drift as assessed by visual inspection and optical diffraction.

Image Analysis and Three-Dimensional Reconstruction

Several areas from the two micrographs (Fig. 1) were digitized at 25-μm steps, corresponding to a $\sim$5.6-Å sampling interval at the specimen. Digitized images were stored and processed on a VAX 8550 computer (Digital Equipment Corp., Maynard, MA) and displayed on a raster graphics device (model 3400; Lexidata Corp., Billerica, MA). Images of individual particles that did not appear to be distorted, disrupted, or overlapped by neighboring particles were extracted from the digitized area using a circular-shaped mask. The diameter of the mask was made large enough to include the spike features visible in the highly defocused micrograph (Fig. 1 a). However, the close packing of particles in the sample imaged closer to focus (Fig. 1 b) necessitated the use of a mask of smaller diameter that excluded portions of some of the spikes at the particle periphery. Subsequent discussions and illustrations concerning the structure of the spike are based on analysis of the micrograph that was defocused $\sim$3 μm, whereas details of the outer capsid surface and all internal features are more clearly revealed in the data obtained from the micrograph defocused by $\sim$0.8 μm. All images were floated (DeRosier and Moore, 1970) and processed to remove uniformly varying gradients in the background (Aebi, 1977) arising from variation in the thickness of the supporting vitreous water. Density values, clearly attributable to neighboring particles not excluded by the mask, were manually adjusted to the average density of the surrounding vitreous water.

The translation (center or origin point) and view orientation (θ, φ, ω; Klug and Finch, 1968) parameters for each virion image were carefully refined using cross-correlation (Olson and Baker, 1989) and common lines procedures (Crowther, 1971; Fuller, 1987; Baker, Drak, and Bina, 1988). Several steps were taken to optimize the refinement of these parameters. Calculations were performed using only a portion of the Fourier transform of the masked image (between 1/280 Å^{-1} and 1/45 Å^{-1}) to minimize noise arising from features in the images that did not correlate with the expected icosahedral symmetry of the virus particles and to exclude low resolution data ($<1/280$ Å^{-1}) that only contributes spherically symmetric information. The Fourier transforms were subdivided into several concentric annuli, and those data weaker than empirically determined thresholds (typically set equal to or greater than the average transform amplitude for each annulus) were also not used in the calculations. This further improved the sensitivity and reliability in refining orientation and translation parameters.

Refinement of the particle parameters was performed in a step-wise, iterative fashion, using progressively more particle images and higher resolution data in each cycle to achieve reliable convergence of the data at the highest available resolution. The essential feature of this procedure involves the initial determination of individual particle orientations on a coarse grid (1° increments of θ, φ, ω) in a search over an icosahedral asymmetric unit ($\theta = 69 - 90$°; $\varphi = -32 - 32$°; $\omega = 0 - 180$°), followed by repeated interparticle refinements using cross-common lines procedures with suc-
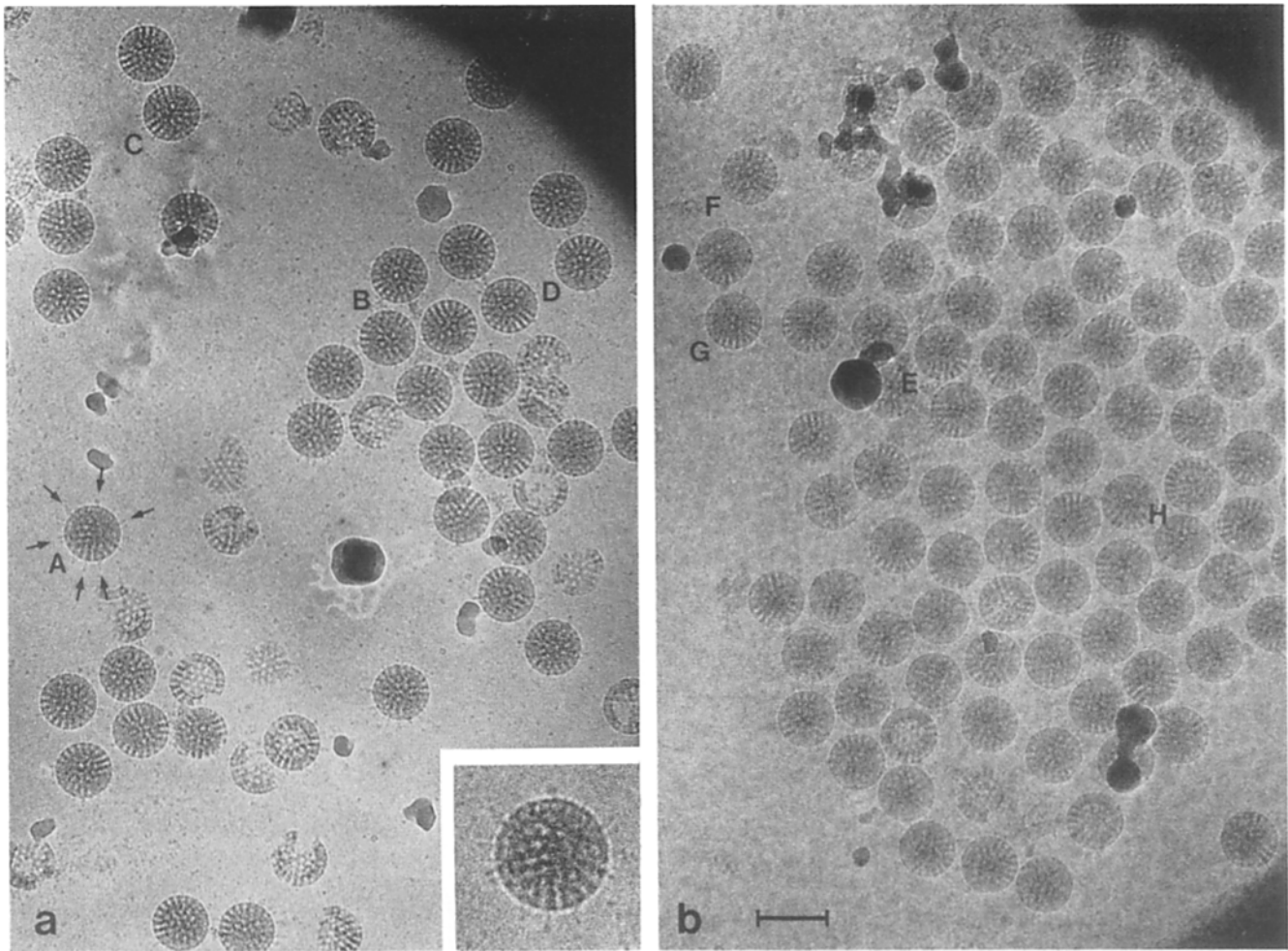
Figure 1. Electron micrographs of unstained, frozen-hydrated RRV samples. The circular outlines and constant diameter of the intact virions indicate good preservation of the spherical shape and symmetry. The presence of spikelike extensions projecting from the virion surface is more apparent in the higher contrast image (*a*) which was recorded at ~3-μm underfocus (compared to ~0.8 μm in *b*). Arrows in *a* identify several spikes on particle A (also shown at 2× higher magnification in the inset). Spikes are observed in other virions on closer inspection. The dense particle packing and weak phase-contrast in image (*b*) tend to obscure the spikes. Distinct differences in the projected virion images indicate that the particle orientations in the frozen sample are approximately random. Selected virions (labeled at the lower left of each particle) are also identified in Figs. 2 and 3 and in the text. Digitized images of 26 different virions from *a* and 28 from *b* were independently combined to compute two separate three-dimensional reconstructions. The contrast in both images has been photographically enhanced. Bar, (*a* and *b*) 1,000 Å.

cessively finer grid sampling intervals (Fuller, 1987). The center of each particle was separately redetermined after each cycle of orientation refinement unless there was no significant change in the θ, φ, and ω values (~0.25° for refinement of data at ~30-Å resolution). The alternating cycles of origin and orientation refinement were repeated until a sufficiently large number of self-consistent particle images were included in the data set and both intra- and interparticle common line phase residuals did not show further improvement.

Independent, three-dimensional reconstructions were computed from each of the two micrographs (Fig. 1) by combining the best data (i.e., those with the lowest common lines phase residuals) from each of the micrographs (26 particles in Fig. 1 *a* and 28 particles in Fig. 1 *b*), using Fourier-Bessel techniques (Crowther, 1971). The resolutions of the two reconstructions were respectively restricted to 37 Å and 26 Å, in part because of limitations imposed by the contrast transfer function characteristics of the electron microscope (Erickson and Klug, 1971) and in part due to the overall noise level in the images. Since the three-dimensional reconstruction has a defined center, the translational alignment of each particle was more accurately refined by cross-correlating each image with the density of the reconstruction, projected in the appropriate viewing direction (Olson and Baker, 1989). This alignment procedure helped improve the interparticle refinement of the

orientation angles and resulted in a more reliable three-dimensional density map. Reconstructions with full icosahedral 532 symmetry were produced using a real space interpolation routine (Fuller, 1987) that imposes the appropriate three-fold symmetry on the map initially calculated with 522 symmetry (Crowther, 1971). All surface-shaded representations were computed at a threshold density level slightly greater than the value at which the highest density gradient occurred. The steepest density gradient should occur at the boundary between virus and solvent. The chosen boundary level slightly reduced the solvent-excluded volume for the virus particle but significantly reduced noise. This was especially evident at the outer capsid surface in regions between the spikes; disconnected "islands" of density were removed while maintaining plausible continuity of the prominent structural features.

Results

Micrographs of frozen-hydrated samples of RRV were recorded at various levels of defocus (Fig. 1). The circular outline and constant diameter of intact particles indicate that the
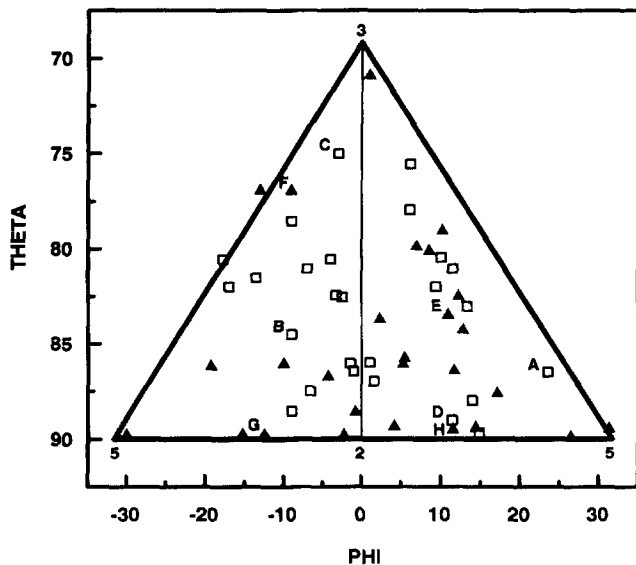
Figure 2. Plot of the refined θ, φ orientation angles for the RRV images used to compute the 37-Å (▲) and 26-Å (□) resolution reconstructions. All orientations are referenced to a single icosahedral asymmetric unit (1/60th of an icosahedron) bounded by one two-fold (θ, φ = 90, 0), one threefold (θ, φ = 69.09, 0), and two fivefold (θ, φ −31.72, 0, and +31.72, 0) axes of symmetry. The plot demonstrates that the data encompass a fairly uniform distribution of orientations. Labeled symbols identify viruses appearing in Figs. 1 and 3. Virions oriented with the same θ angle but with opposite φ angles exhibit mirror symmetric projected images.

spherical shape of the virus is well preserved by the specimen preparation techniques. The spokelike features in individual particle images are clearly evident. Distinct differences in the appearance of individual particle images indicate that the virion orientations in the frozen-hydrated specimen are approximately random.

In highly underfocused images (Fig. 1 *a*), faint, spikelike features are observed which project radially outward from the outer capsid. Many spikes extend >100Å from the particle periphery (c.f., particle A in Fig. 1 *a* and *inset*). These spikes were not previously observed in negatively stained or in fixed and embedded virus specimens. Their existence was recently demonstrated in cryoelectron microscopy studies of rotavirus strain SA11 (Prasad et al., 1988). Spikes are more difficult to discern in images recorded close to focus (Fig. 1 *b*) primarily because of the weak phase-contrast in such images. Furthermore, in specimens in which virions are closely packed (Fig. 1 *b*), the spike features are obscured due to overlapping density between neighboring particles.

Reliable determination of the three-dimensional structure of RRV requires the combination of data from several virions in different orientations (Crowther, 1971). (An implicit assumption is that, aside from differences in orientation, all virions in the frozen-hydrated sample are identical.) The refined orientations (θ, φ) for the two data sets (Fig. 2) display fairly uniform distributions of particle views from which the two reconstructions were computed.

The reliability of features in each of the reconstructions was visually assessed by comparing individual particle images with corresponding views of the reconstruction ob-

tained by back-projection of the density map in the same orientation as the particle (Fig. 3). Such comparisons reveal close correspondence between the respective, prominent features. Self-consistency between the separate particle data sets from the two micrographs is clearly illustrated by comparing the original images for particles D and H and their respective back-projected views (displayed in Fig. 3 with the same ω angle). Both particles, although from different samples imaged at different defocus levels, were fortuitously frozen in nearly identical orientations and have nearly identical back-projected views. These qualitative assessments provide evidence that the individual images were correctly combined to produce the three-dimensional density maps.

The extent to which individual particle images display the expected icosahedral symmetry was quantitatively tested by computing the mean phase difference between pairs of common lines in the Fourier transform of each digitized image. As expected, the mean amplitude-weighted phase error (Fig. 4) for both reconstructions increases at higher resolution as the noise level increases. The phase errors are <90° at the resolution limits of the reconstructions and are significantly less for most of the data. Thus, icosahedral symmetry is well preserved in the particles included in the three-dimensional reconstructions.

An additional measure of the reliability of the reconstructions was obtained by quantitatively comparing reconstruc-
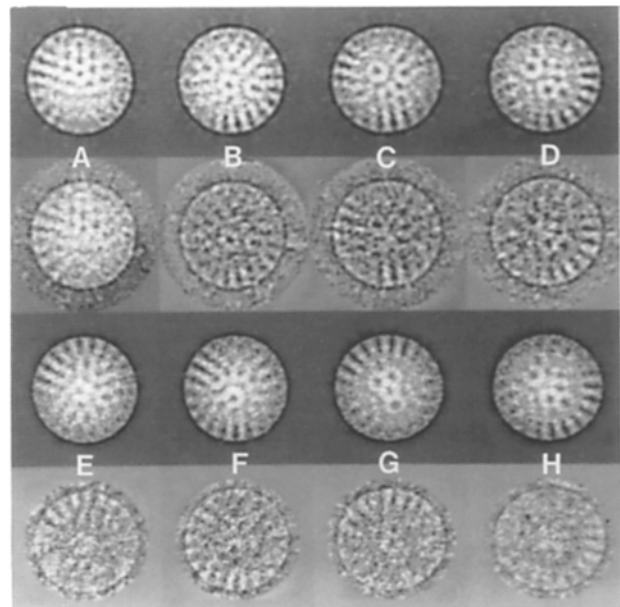

Figure 3. Comparisons of original virion images (*bottom of each pair*) with corresponding projected views of the three-dimensional reconstructions (*top of each pair*). The close correspondence between respective image pairs provides a stringent qualitative check on the validity of the three-dimensional reconstructions. Particles labeled *A–D* are from the first data set (Fig. 1 *a*) and *E–H* are from the second data set (Fig. 1 *b*). All images are displayed with reverse contrast so that the brightest features correspond to regions of greatest mass density. To improve the visibility of features, the unprocessed images were Fourier-filtered to remove both low (<1/200 Å⁻¹) and high (>1/30 Å⁻¹) frequency noise, and the contrast was stretched using a linear scale factor.
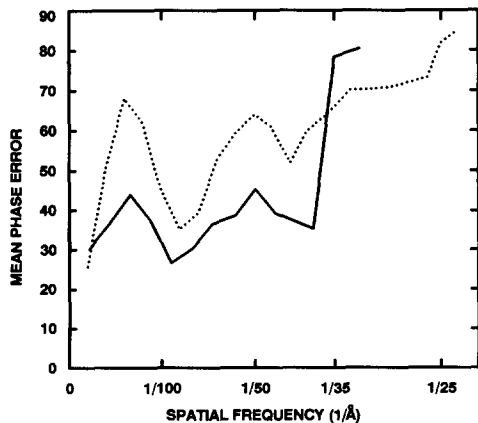
Figure 4. Plots of the mean weighted phase errors as a function of spatial frequency for the 37 Å (———) and 26 Å (· · · · · ·) resolution data sets. Mean phase errors for each data set, weighted by the mean Fourier amplitude at each spatial frequency tested, were evaluated by computing the average phase difference for all pairwise particle comparisons at regular intervals along common points (cross–common lines) in the respective particle Fourier transforms (Fuller, 1987). Large phase errors (approaching 90°) signify poor correlation of the data with icosahedral symmetry. The resolution limits of the two data sets are consistent with the defocus level of the micrographs (Fig. 1).

tions computed from independent, half-data sets. The 26 particle data set for the 37-Å resolution reconstruction was randomly subdivided into four different pairs of independent 13 particle data sets. Reconstructions for all eight half-data sets were computed with 522 symmetry, and the phase differences between the Fourier transforms of independent pairs of reconstructions were computed as a function of spatial frequency (Fig. 5). The phase differences are <35° out to a spatial frequency of 1/37 Å^{-1} (Fig. 5), indicating excellent agreement between the reconstructions in each pair. Surface-shaded views of two such reconstructions (Fig. 6, a and b), corresponding to data sets represented by the solid line in Fig. 5, display remarkably similar features even in regions where the density approaches the noise level. Close correspondence between these subtle features, such as the dimensions and complex morphologies of the spikes and holes, provides additional confidence that genuine features of the virion structure were reliably determined at moderate resolution. Reconstructions from two of the half-data sets (Fig. 6, a and b) can be compared with the full 26 particle data set with either 522 (Fig. 6 c) or full icosahedral 532 symmetry (Fig. 6 d). Doubling the number of particle images in the reconstruction (i.e., 26 vs. 13) theoretically reduces the noise level by $\sqrt{2}$ (compare Fig. 6, a and b with c). Thus, the reliability of the 26 particle reconstruction should exceed that of the half-data set reconstructions, as depicted in Fig. 5. The density map with full icosahedral symmetry (Fig. 6 d) is visually indistinguishable from the map with lower symmetry (Fig. 6 c). This provides further evidence that the virions are icosahedral and the symmetry is well preserved.

The outer surface of RRV, viewed along icosahedral two-, three-, and fivefold axes of symmetry in the 37-Å resolution reconstruction, displays several prominent features (Fig. 7). 60 spikes project radially from the smoothly rippled, nearly spherical outer capsid surface. The outer shell is penetrated

by 132 holes, of three types (following the nomenclature of Prasad et al., 1988): 12 type I holes at the fivefold vertices, 60 type II holes at peripentonal positions (adjacent to the vertices), and 60 type III holes surrounding the icosahedral threefold axes. Type I holes are nearly circular and are smaller (~40 Å in diameter) than those of either types II or III, which are approximately crescent shaped with a widest dimension of ~65 Å. The 60 spikes are situated at the edges of the type II holes, distal to the type I holes. The $T = 13$ symmetry of the outer capsid (fivefold axes separated by three local sixfold symmetry axes as shown in Fig. 7 b) was not enforced by the reconstruction procedures and is clearly evident from the distribution of the holes.

The internal structure of RRV is revealed in equatorial sections (infinitely thin slice through the particle center) of the two three-dimensional reconstructions (Fig. 8). The overall features in both reconstructions are quite similar, although finer details are apparent in the map at higher resolution. In cross section, the structure appears to be composed of two, roughly spherical shells of density at high radii (377 and 299 Å), connected by pillars or columns of density. A third, non-spherical shell of density resides at a lower radius (255 Å) just outside the nearly featureless nucleic acid core. The three prominent density shells are clearly identified in plots of the spherically averaged reconstruction density (Fig. 9). The holes at the virion surface (Fig. 7) open into wide cavities between the outer and inner capsid shells and appear to completely extend to the core. The cross-sectional views (Fig. 8) give an impression that the virion is penetrated by distinct tubelike channels that extend radially from the holes at the surface to the core region. In fact, aqueous cavities ex-
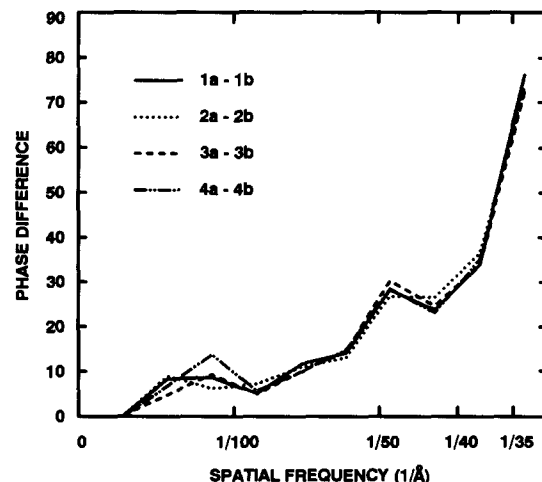

Figure 5. Quantitative comparisons of four independent pairs of three-dimensional reconstructions. The 26 particles in the first (37-Å resolution) data set were randomly subdivided four times into pairs (a and b) of unique half (13-particle) data sets, distinguished in the plot by four distinct lines. The particle orientation parameters were independently refined for each of the eight half-data sets, and then separate reconstructions were computed. Low phase errors (<35°), computed from differences between the Fourier transforms of each of the corresponding pairs of reconstructions, provide strong evidence for self-consistency among the data and indicate that the reconstructions are quite reliable to the resolution limit of the data.
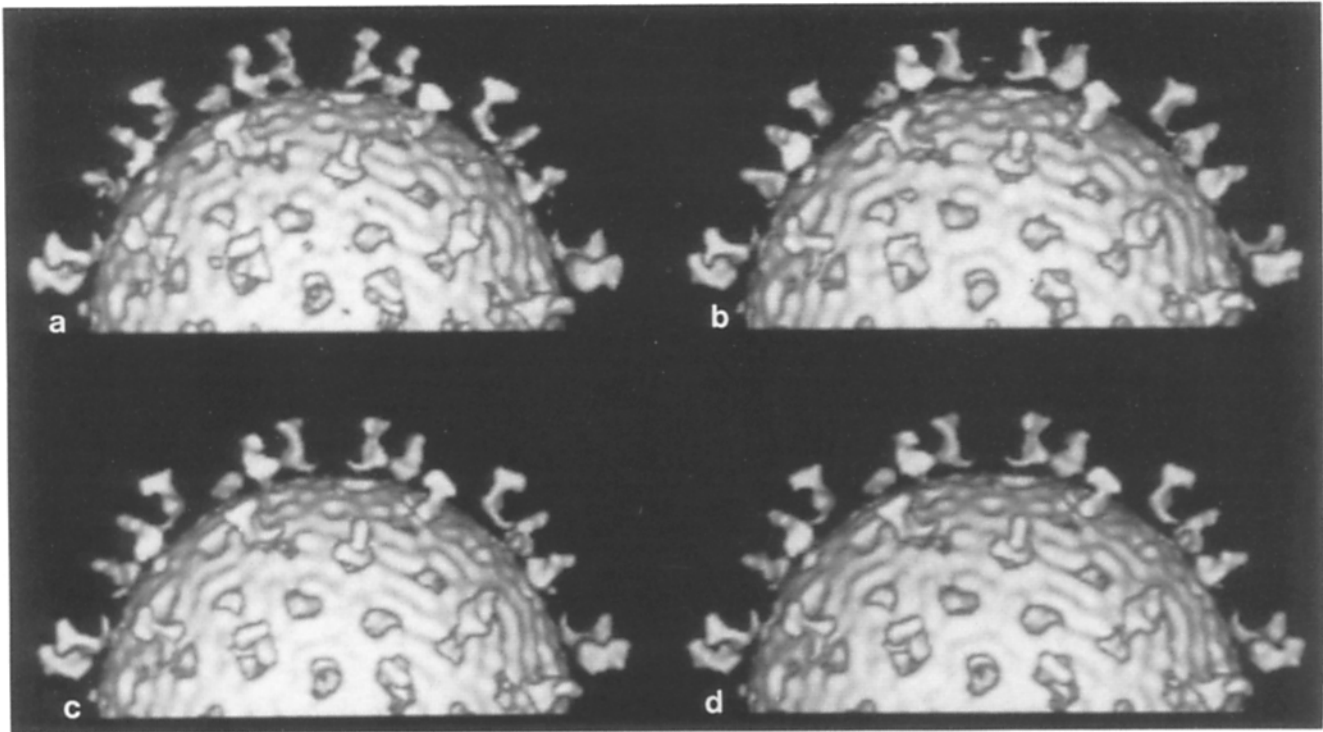
Figure 6. Comparison of four reconstructions, two computed from independent half (13 particle) data sets in which 522 symmetry was imposed (*a* and *b*), and two computed from the full, 26 particle data set with either 522 (*c*) or 532 (*d*) symmetry. The top half of each reconstruction is displayed with a surface-shaded representation. The reconstructions in *a* and *b* correspond to the pair identified by the solid line in Fig. 5. The excellent agreement between the different 37-Å resolution reconstructions for both prominent and subtle surface features provides strong evidence that genuine features in the RRV structure are revealed.

tend in both radial and azimuthal directions beneath the outer capsid surface, creating an interconnecting network of aqueous cavities (see Discussion).

Discussion

We have used cryoelectron microscopy and image reconstruction techniques to examine the three-dimensional structure of RRV. The salient features of the $T = 13l$ icosahedral virions are best illustrated in surface views of the reconstruction, obtained by truncating the density map at successively smaller radii (Fig. 10). RRV consists of a complex, highly organized structure characterized by several distinct features: (*a*) prominent spikes that radiate from the outer capsid; (*b*) two concentric capsid shells, both perforated by similarly sized holes that are in register; (*c*) pillars of density that interconnect the capsid shells; and (*d*) a central nucleic acid core region bounded by a third shell of density.

Outer Capsid

Spikes Have Complex Morphology and Project >100 Å from the Outer Capsid Surface. The most striking aspect of the outer surface of RRV is the 60 spikes, which appear to be attached to the surface of the outer capsid near the edge of the peripentonal (type II) holes and extend at least 100 Å above the surface. Details of the spike structure are best revealed in the lower (37 Å) resolution reconstruction since the procedure used to select particle images in the higher resolu-

tion (26-Å) data set necessitated truncation of features at radii >40 Å outside the outer capsid surface (see Materials and Methods). Therefore, the distal ~60–80 Å of the spikes could not be observed in the 26-Å reconstruction. However, the proximal ends of the spikes appeared with nearly identical morphologies in both reconstructions (data not shown). The spikes have a complex morphology (Fig. 11), consisting of a bilobed "head" (~40 × 40 × 75 Å), connected to a triangular shaped "body" (~30 Å thick, 70 Å high, and 80 Å wide at the base) from which a narrow "tail" (~53 Å long and 25 Å in diameter) extends over the peripentonal type II hole. (Note that the stated dimensions are subject to errors due to (*a*) the finite resolution of the density map; (*b*) the choice of cut-off level that establishes the boundary between the virion and regions containing vitreous water; (*c*) inherent inaccuracies of micrograph magnification calibrations; and (*d*) possible loss of some spikes during virus purification.) The long axes of the head and tail are approximately parallel to each other and perpendicular to the base of the body. Each spike appears to be attached to the outer capsid surface via a thin stalk of density connecting the proximal end of the tail to the edge of the peripentonal hole. These connections may appear anomalously thin as a result of Fourier termination artifacts generated by the strong Fresnel defocus fringe present at regions of the structure where steep density gradients occur (e.g., at the interface between the capsid surface and the surrounding layer of vitreous water). However, the same characteristic feature is observed in both reconstructions (data not shown), computed from images at different defocus settings,
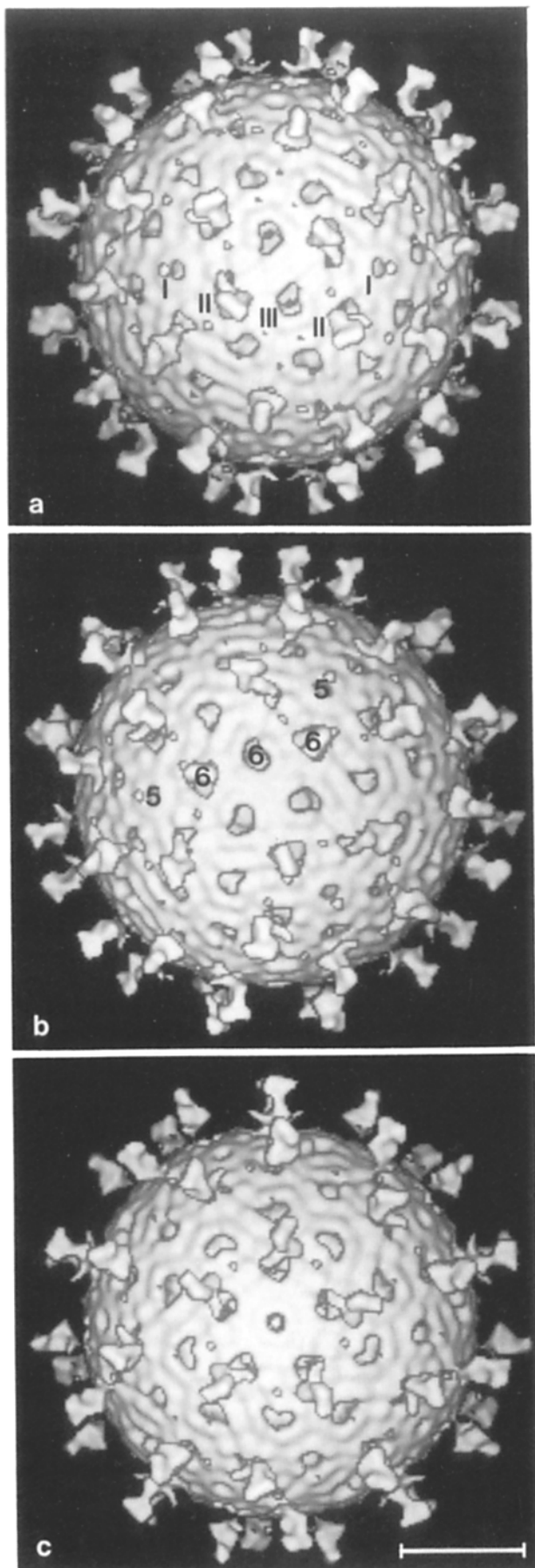
so that the spikes may indeed be attached to the outer capsid surface via a slender "stalk."

The spikes of RRV and those observed in a previous reconstruction of strain SA11 (Prasad et al., 1988) differ significantly in both size and morphology. SA11 spikes appear as short, stublike protrusions that are wider at the base and only extend ~45 Å from the outer capsid surface compared to >100 Å for RRV spikes. A new reconstruction of strain SA11 (Prasad et al., 1990) displays surface spikes more closely resembling those in Fig. 11. The short, stubby appearance of the spikes in the previous SA11 reconstruction was attributed to noise in the density map (Prasad et al., 1990). The spikes in both RRV and SA11 are undoubtedly longer than that revealed in the respective reconstructions as is evident in unprocessed images of both RRV (Fig. 1 a, inset) and SA11 (Fig. 1; Prasad et al., 1988). If the spike protein is flexible, the distal ends may adopt distinct conformations or move freely in solution and thus would be smeared out by the computer averaging procedures. In addition, contrast in the spike feature would also be reduced by averaging if the virions that were processed did not contain a full complement of 60 spikes as a result of loss during isolation procedures.

The extended morphology of the spike may facilitate binding interactions with cellular receptors. The bilobed appearance of the "head" suggests a multidomain or dimeric subunit structure for the hemagglutinin of rotavirus, as has been reported for two other animal viruses: the trimeric influenza hemagglutinin (Wilson, Skehel, and Wiley, 1981) and the tetrameric reovirus hemagglutinin (Bassel-Duby et al., 1987). A recent reconstruction of SA11 virions complexed with Fab fragments directed against VP4 revealed two Fab molecules bound to each spike (Prasad et al., 1990). The estimated volume for each spike was consistent with a VP4 dimer. These structural results suggest that the rotavirus hemagglutinin is present in a dimeric state (Prasad et al., 1990). However, there is no biochemical evidence supporting an oligomeric arrangement of the viral hemagglutinin of rotavirus. In fact, densitometry measurements from Coomassie-stained polyacrylamide gels of rotavirus SA11 (Liu, Offit, and Estes, 1988) predict a stoichiometric ratio of VP4 to VP7 of 1:55, much lower than expected on the basis of symmetry considerations and inspection of the three-dimensional density maps:

$[60n$ copies of VP4: $(60 \times 13$ copies of VP7$)] = n{:}13$, where n is the number of copies of VP4 per spike.

Figure 7. Surface views of the 37-Å RRV reconstruction viewed along twofold (a), threefold (b), and fivefold (c) symmetry axes display $T = 13$ icosahedral lattice symmetry. The characteristic features of the outer surface of RRV are the 60 prominent spikes extending over 100 Å from the virion surface and a relatively smooth, spherical outer capsid perforated by 132 holes of three types (identified by labels in a): 12 type I holes at the icosahedral vertices; 60 type II holes at the peripentonal positions; and 60 type III holes encircling the icosahedral threefold axes of symmetry. The reconstructions are displayed as the left-handed enantiomorph based on the analysis of freeze-dried, platinum-shadowed rotavirus samples (Roseto et al., 1979). Labels in b identify the 5- and 6-coordinate positions that lie between one pair of vertices in the $T = 13l$ icosahedral surface lattice. Bar, 250 Å.
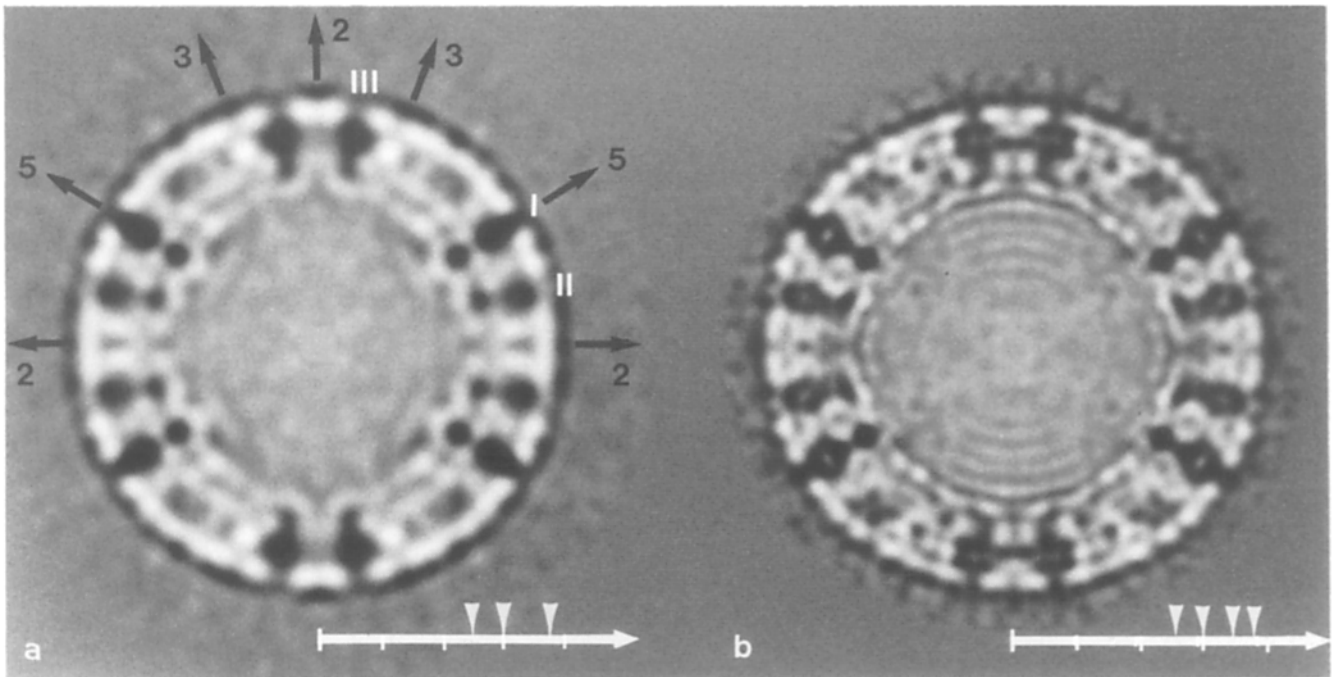
Figure 8. Central (equatorial) sections of the 37 Å (*a*) and 26 Å (*b*) reconstructions viewed along a twofold direction are displayed with reverse contrast (bright regions correspond to high mass density). The three types of holes identified in Fig. 7 *a* are labeled in *a*. Icosahedral symmetry axes that lie within the equatorial plane are also shown in *a*. The dominant structural features are quite comparable in the two reconstructions. As expected, the higher resolution reconstruction (*b*) displays finer definition of the detailed morphological features. Spikes are not apparent in this view since they are not contained within the limited confine of a thin, equatorial slice viewed along a twofold direction. Also, only the type I holes are centered within an equatorial slice; the centers of the type II and III holes lie outside this plane. In this view, the RRV structure appears to consist of five distinct and approximately concentric layers: outer capsid shell, radial pillars, inner capsid shell, and a core shell that surrounds a relatively uniform region of density, presumably corresponding to the segmented RNA genome. Since the bulk of the RNA is not expected to be organized with the icosahedral symmetry of the outer layers, density values inside a radius of ~235 Å were multiplied by a radial smoothing function to reduce the noise that characteristically increases toward the center of icosahedral reconstructions. Arrowheads identify the radial positions of density peaks in the two central sections that correspond to the three prominent shells in *a* and *b* and the pillars in *b* (see also Fig. 9). Radial fiducial marks indicate 100 Å divisions.
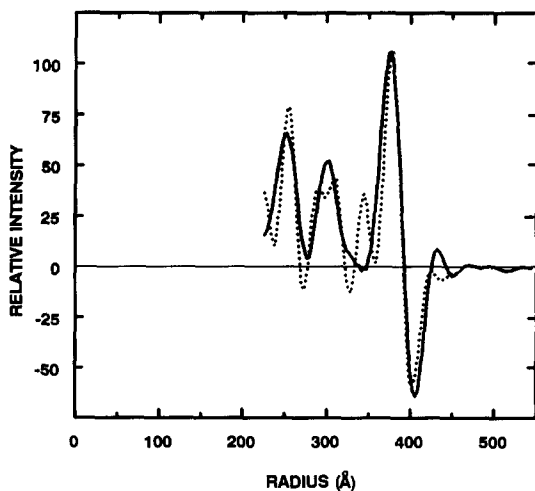

Figure 9. Radial density plots of the 37 Å (———) and 26 Å (· · · · ·) resolution reconstructions illustrating the three-shelled structure of RRV. Peaks of mass at radii of 377, 299, and 255 Å correspond respectively to the outer, inner, and core capsid shells as identified in the equatorial slices (Fig. 8). The peak at a radius of 359 Å in the 26-Å resolution plot corresponds with the density attributed to the pillars that bridge the inner and outer capsid shells. The density corresponding to the outer capsid spikes (radii from

These data suggest that the spike is likely to be composed primarily if not completely by the VP4 polypeptide. Moreover, if correct, these data might also suggest that the 60 icosahedrally related positions may not be fully occupied by VP4 molecules. Further experimentation, such as biochemical cross-linking analysis and higher resolution structural studies, may reconcile the discrepancies between the biochemical and structural results.

Outer Capsid Shell Consists of VP7 Molecules Arranged Around 132 Holes. The second prominent feature of the RRV outer capsid is the presence of 132 aqueous holes. The characteristic ($T = 13$) distribution and approximate dimensions of the holes are comparable to those observed in SA11 (Prasad et al., 1988). The similarities in the sizes and asymmetrical shapes of the type II and III holes, and the observation that the type I holes are smaller in size and more symmetrical in shape, indicate that the major outer capsid protein, VP7, is packed within the shell in at least two dis-

~393–505 Å) is obscured in the radial density plots because of the strong Fresnel defocus fringe just outside the outer capsid surface and because vitreous water accounts for >95% of the volume in this region. The plots were normalized by assigning the same value to the maxima at 377 Å.
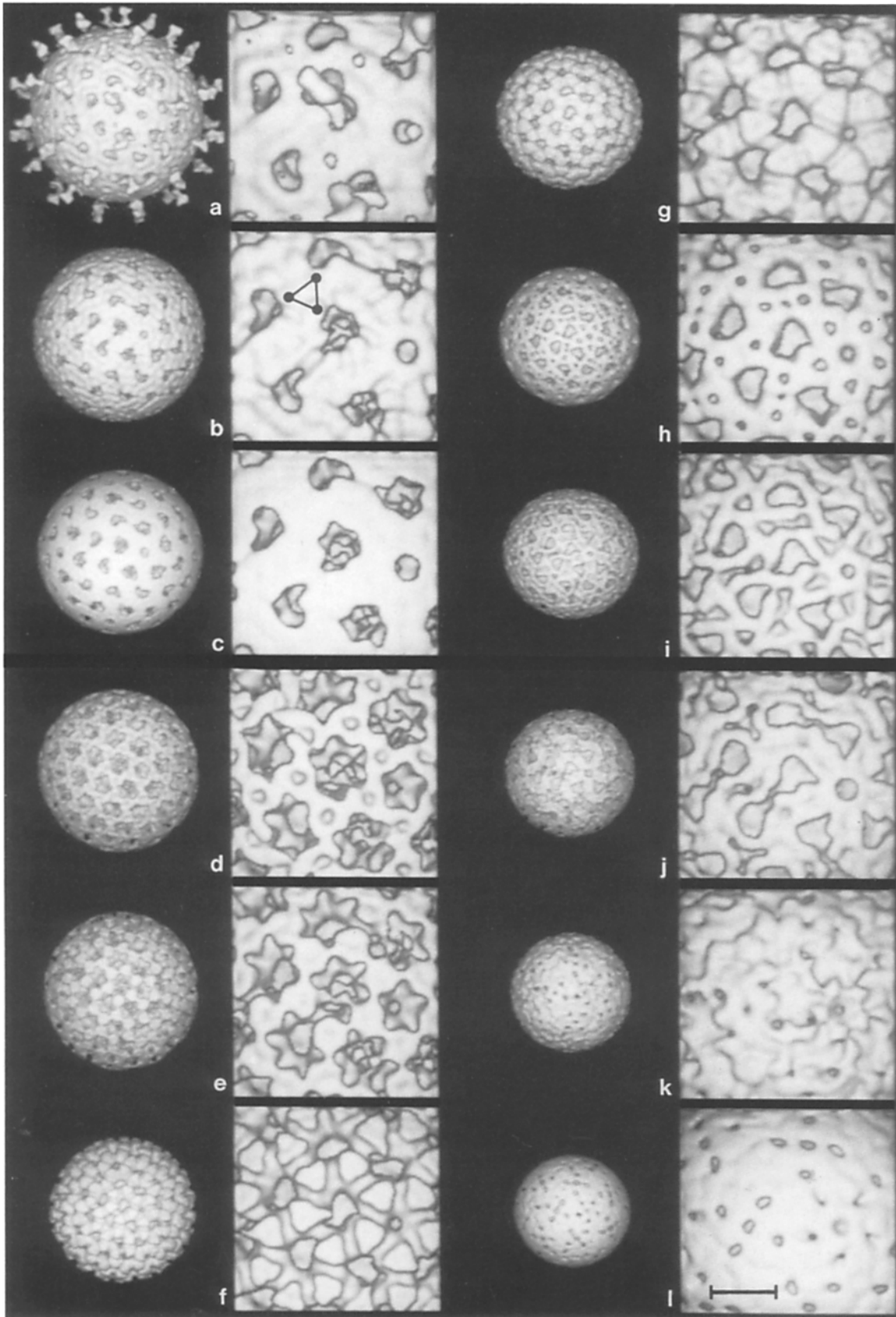
Figure 10. Surface-shaded representations of the RRV reconstructions viewed at successively smaller radii, obtained by truncating the three-dimensional maps with spherical envelopes to reveal the internal structure. All surface views are from an equatorial direction, close to the axis of a type II hole ($\theta = 90$, $\varphi = 15$) and have been calculated at the same threshold density. All views except *a* are from the 26-Å resolution map. Fine details are revealed in the enlarged central region of each full view. One triangular motif, presumed to be a trimeric aggregate of VP7 molecules situated in the outer capsid, is schematically labeled in *b*. The radii corresponding to the different levels are (*b*) 393 Å; (*c*) 377 Å; (*d*) 365 Å; (*e*) 353 Å; (*f*) 335 Å; (*g*) 324 Å; (*h*) 312 Å; (*i*) 300 Å; (*j*) 288 Å; (*k*) 271 Å; and (*l*) 259 Å. Bar, (for close-up views shown in *l*) 100 Å.
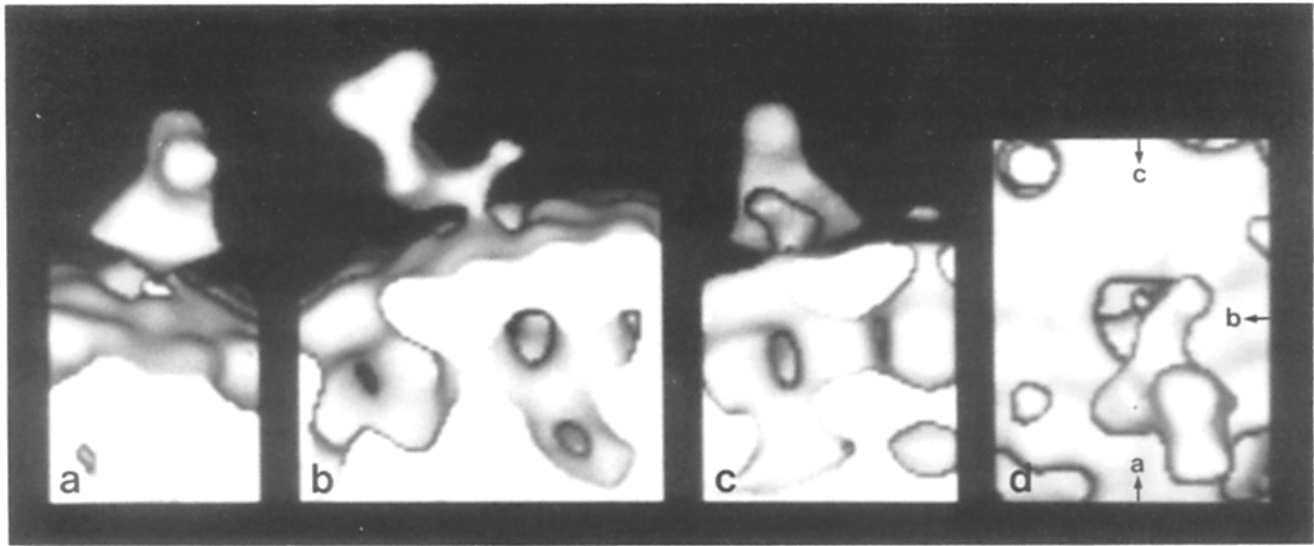
Figure 11. Magnified views of the RRV outer capsid spike. Side views (*a*, *b*, and *c*) reveal a bilobed head attached to a triangular shaped body from which a thin tail extends. The spike attaches to the outer capsid via a slender stalk at the edge of the peripentonal (type II) holes. The interconnected network of aqueous cavities between the outer and inner capsids is clearly depicted in *b* and *c*. The top view *d* shows that the tail extends across the opening of the type II hole. The directions of the "edge-on" views (*a*, *b*, and *c*) relative to the "top-view" (*d*) are indicated in *d*.

tinct arrangements. Inspection of the outer capsid surface reveals a closely packed network of 260 triangular-shaped motifs. (One such motif is schematically identified in Fig. 10 *b*.) Each motif is ~84 Å on edge and consists of three globular features at the corners of an approximate equilateral triangle, interconnected by rod-shaped regions of density. The distinct morphology observed for each of the subunits of the trimeric motif suggests that VP7 may exist as a multi-domain polypeptide in the outer capsid. Five globular "domains" closely associate in an annular ring to define the edge of the smaller, type I holes at the twelve icosahedral vertices. The asymmetric shapes of the type II and type III outer capsid holes indicate that the arrangements of chemically identical VP7 molecules lack the local sixfold symmetries expected for a quasi-equivalent structure (Caspar and Klug, 1962).

Since VP7 and VP4 are the major outer capsid proteins and the estimated volume occupied by VP7 is ~20 times greater than that for VP4 (Liu, Offit, and Estes, 1988), the smoothly rippled outer capsid surface is interpreted as being formed primarily by VP7 molecules, each of which appears to consist of at least two distinct (globular and rod-shaped) domains. Based on the contouring of the density map that defines the boundaries of the nonaqueous regions, the volume of the solvent-excluded density (accounting for 75% of the volume) between radii of 365 and 392 Å is ~3.6 × 10⁷ Å³. A total of 780 copies of VP7, consistent with the stoichiometry expected for a $T = 13$ icosahedral model, would occupy ~3.26 × 10⁷ Å³ (assuming VP7 has a partial specific volume of 0.74 cm³/gm, a value typical for most soluble, globular proteins). This accounts for ~90% of the density within the defined spherical shell of the outer capsid. The remaining density may be attributed to portions of the VP4 and VP6 molecules since they probably form close associations with VP7.

Inner Capsid

Trimeric Pillars Connect the Inner Capsid Surface with the Outer Capsid Shell.

At a radius of 360 Å, just beneath the outer capsid shell, there are 260 pillar-shaped features that give rise to the characteristic bristlelike inner capsid structure, closely resembling the three-dimensional reconstruction of single-shelled particles of SA11 (Prasad et al., 1988). In the radial density plot (Fig. 9), the pillars correspond to the peak of density in the 26-Å resolution plot centered at a radius of 359 Å. This location is identified by an arrow in the central section views (Fig. 8 *b*). The pillars are ~50 Å in diameter and extend a distance of ~47 Å between the inner surface of the outer capsid and the base of the inner capsid (Fig. 10). Near the base of each pillar at a radius of 324–335 Å (Fig. 10, *f* and *g*), the density has a distinctly triangular-shaped cross section, suggesting a trimeric subunit association. This is consistent with a model in which each pillar is formed by the association of three copies of VP6, the major inner capsid protein (Gorziglia et al., 1985). This model is also supported by previous observations of trimeric structures in hexagonal arrays from disrupted virions (Martin, Palmer, and Middleton, 1975) and tubelike aggregates that apparently form spontaneously in viral preparations (Esparza and Gil, 1978). At a radius of 365 Å, the trimers appear to have a central indentation or hole (Fig. 10 *d*). The large cavity beneath each type I hole of the outer capsid is bounded by five trimeric pillars. Similarly, the cavities beneath the type II and III holes are formed by rings of six pillars.

Smooth Inner Capsid Shell Contains 132 Holes in Register with the Outer Capsid Holes.

At the base of the pillars (~312-Å radius) lies a smooth spherical surface, perforated by 132 holes in radial register with the three types of outer

capsid holes (Fig. 10 *h*). The type I inner capsid holes are smaller than those in the outer capsid, whereas the type II and III holes have roughly equivalent sizes but slightly different shapes in the respective capsids. Since the two capsid shells have approximately the same thickness ($\sim$30 Å), there must be considerably less mass in the inner capsid shell compared to that in the outer capsid. The radial density plots (Fig. 9) are consistent with this observation since the peak corresponding to the radius of highest mean density in the inner capsid shell (at 299-Å radius) is $\sim$40% smaller than the peak attributed to the outer capsid shell (at 377-Å radius).

The distribution of viral proteins within the inner capsid has not been established. If there are 780 copies of VP6 forming the 260 trimeric domains, then the estimated volume occupied by VP6 is 3.9×10^8 Å^3. The volume of the solvent-excluded density (accounting for 47% of the volume) in the region of the pillars that interconnect the outer and inner capsid shells (radii of $\sim$318–365 Å) is $\sim$3.2 $\times$ 10^7 Å^3. Thus, VP6 likely constitutes the entire "pillar" structure and may also form part of the smooth inner capsid shell. The presence of other viral proteins (VP1, VP2, VP3) within or in association with the inner capsid structure, must also be considered.

Virus Core

The third major peak in the radial density plot (Fig. 9), at a radius of 255 Å, resides just outside the nucleic acid core and corresponds to a third shell of density. The central sections (Fig. 8) and the surface view at 271 Å (Fig. 10 *k*) both indicate that this third shell appears distinctly nonspherical and is readily distinguished from the smooth inner capsid shell. Published images of negatively stained, chemically disrupted rotaviruses display subviral particles with an angular morphology and a size comparable to the third shell displayed in Fig. 10 *k* (Bican et al., 1982; Palmer, Martin and Murphy, 1977; Ludert et al., 1986). Biochemical analysis indicates that these angular structures contain VP1, VP2, and VP3 so that these proteins may represent the principal components of the shell which encapsidates the RNA genome. A prominent feature of the core capsid surface (Figs. 10, *k* and *l*) is the shallow depression at each of the 12 icosahedral fivefold axes, suggesting that the cavities beneath the type I holes extend radially inwards to a greater extent than either of the cavities below the type II or type III holes. The space corresponding to the type II and III holes might be occupied by proteins (e.g., VP1, VP2, and VP3) or organized RNA.

Structural Relationships between the Two Outermost Capsids of RRV

The two most prominent capsids of RRV may be simply described as consisting of two spherical shells, each perforated by 132 holes arranged in radial register. The shells appear to be connected by 260 radially directed, trimeric-shaped pillars. Consequently, the RRV structure consists of an interconnected network of aqueous cavities that appear to provide free access to all of the holes in both capsid shells. The existence of 132 independent, tubelike channels is therefore not apparent in RRV. Holes at the outer surface of the virion (Fig. 10 *b*) open into wide cavities formed by the five and six coordinated groups of pillars beneath the outer capsid

shell. Gaps between adjacent pillars provide pathways that interconnect the cavities. The mechanism by which the segmented RNA genome is transmitted to target cells is unknown. The extensive aqueous network provides ample space for the egress of RNA as well as for diffusion of ions, metabolites, or other small molecules such as nucleotides. Determination of how such processes occur, whether by passive diffusion or active translocation of molecules along specific pathways, awaits further investigation.

Conclusions

The icosahedral structure of RRV closely resembles the basic features of strain SA11 (Prasad et al., 1988, 1990), and our analysis reveals several additional features. The sixty spikes attributed to VP4, have a complex, bilobed morphology and extend over 100 Å above the smoothly rippled surface of the outer capsid, believed to consist primarily of VP7. Pillars, attributed to trimeric oligomers of VP6, provide stabilizing interactions between the outer and inner capsids. The smooth shells of the outer and inner capsids (centered at radii of 377 and 299 Å) are perforated by three classes of holes that are in radial register. The space between the shells, not occupied by the pillars, forms an interconnected aqueous network of cavities. A third layer of density, at a radius of 255 Å, appears to form a "core" shell which encapsidates the RNA genome. Future structural studies of RRV using cryoelectron microscopy and image analysis techniques may provide an objective way to examine the proteolytic events that trigger viral infectivity and also provide insight into the molecular basis of the interactions of rotavirus with target cells and neutralizing antibodies.

References

Aebi, U. 1977. Ph.D. thesis. University of Basel, Basel, Switzerland. 346 pp.

Baker, T. S., J. Drak, and M. Bina. 1988. Reconstruction of the three-dimensional structure of simian virus 40 and visualization of the chromatin core. *Proc. Natl. Acad. Sci. USA.* 85:422–426.

Bassel-Duby, R., M. L. Nibert, C. J. Homcy, B. N. Fields, and D. G. Sawutz. 1987. Evidence that the sigma 1 protein of reovirus serotype 3 is a multimer. *J. Virol.* 61:1834–1841.

Bastardo, J. W., and I. H. Holmes. 1980. Attachment of SA-11 rotavirus to erythrocyte receptors. *Infect. Immun.* 29:1134–1140.

Bican, P., J. Cohen, A. Charpilienne, and R. Scherrer. 1982. Purification and characterization of bovine rotavirus cores. *J. Virol.* 43:1113–1117.

Caspar, D. L. D., and A. Klug. 1962. Physical principles in the construction of regular viruses. *Cold Spring Harbor Symp. Quant. Biol.* 27:1–24.

Chiu, W. 1986. Electron microscopy of frozen, hydrated biological specimens. *Annu. Rev. Biophys. Biophys. Chem.* 15:237–257.

Clark, S. M., J. R. Roth, M. L. Clark, B. B. Barnett, and R. S. Spendlove. 1981. Trypsin enhancement of rotavirus infectivity: mechanism of enhancement. *J. Virol.* 39:816–822.

Crowther, R. A. 1971. Procedures for three-dimensional reconstruction of spherical viruses by Fourier synthesis from electron micrographs. *Philos. Trans. R. Soc. Lond. B Biol. Sci.* 261:221–230.

DeRosier, D., and P. B. Moore. 1970. Reconstruction of three-dimensional images from electron micrographs of structures with helical symmetry. *J. Mol. Biol.* 52:355–369.

Dubochet, J., M. Adrian, J.-J. Chang, J.-C. Homo, J. Lepault, A. W. McDowall, and P. Schultz. 1988. Cryo-electron microscopy of vitrified specimens. *Q. Rev. Biophys.* 21:129–228.

Erickson, H. P., and A. Klug. 1971. Measurement and compensation of defocusing and aberrations by Fourier processing of electron micrographs. *Philos. Trans. R. Soc. Lond. B Biol. Sci.* 261:105–118.

Esparza, J., and F. Gil. 1978. A study on the ultrastructure of human rotavirus. *Virology.* 91:141–150.

Estes, M. K., E. L. Palmer, and J. F. Obijeski. 1983. Rotaviruses: a review. *Curr. Top. Microbiol. Immunol.* 105:123–184.

Flewett, T. H., A. S. Bryden, H. Davies, G. N. Woode, J. C. Bridger, and J. M. Derrick. 1974. Relation between viruses from acute gastroenteritis of children and newborn calves. *Lancet.* 2:61–63.

Flores, J., K. Midthun, Y. Hoshino, K. Green, M. Gorziglia, A. Z. Kapikian, and R. M. Chanock. 1986. Conservation of the fourth gene among rotaviruses recovered from asymptomatic newborn infants and its possible role in attenuation. *J. Virol.* 60:972–979.

Flores, J., I. Perez-Schael, M. Gonzalez, D. Garcia, M. Perez, N. Daoud, W. Cunto, R. M. Chanock, and A. Z. Kapikian. 1987. Protection against severe rotavirus diarrhea by rhesus rotavirus vaccine in Venezuelan infants. *Lancet.* 1:882–884.

Fukami, A., and K. Adachi. 1965. A new method of preparation of a self-perforated micro plastic grid and its application. *J. Electron Microsc.* 14:112–118.

Fukuhara, N., O. Yoshie, S. Kitaoka, T. Konno, and N. Ishida. 1987. Evidence for endocytosis-independent infection by human rotavirus. *Arch. Virol.* 97:93–99.

Fuller, S. 1987. The T=4 envelope of sindbis virus is organized by interactions with a complementary T=3 capsid. *Cell.* 48:923–934.

Gorziglia, M., C. Larrea, F. Liprandi, and J. Esparza. 1985. Biochemical evidence for the oligomeric (possibly trimeric) structure of the major inner capsid polypeptide (45k) of rotaviruses. *J. Gen. Virol.* 66:1889–1900.

Gorziglia, M., Y. Hoshino, A. Buckler-White, I. Blumentals, R. Glass, J. Flores, A. Z. Kapikian, and R. M. Chanock. 1986. Conservation of amino acid sequence of VP8 and cleavage region of 84-kDa outer capsid protein among rotaviruses recovered from asymptomatic neonatal infection. *Proc. Natl. Acad. Sci. USA.* 83:7039–7043.

Graham, D. Y., and M. K. Estes. 1980. Proteolytic enhancement of rotavirus infectivity: biologic mechanisms. *Virology.* 101:432–439.

Holmes, I. H. 1983. Rotaviruses. *In* The Reoviridae. W. K. Joklik, editor. Plenum Publishing Corp., New York. 359–423.

Hoshino, Y., R. G. Wyatt, H. B. Greenberg, J. Flores, and A. Z. Kapikian. 1984. Serotypic similarity and diversity of rotaviruses of mammalian and avian origin as studied by plaque-reduction neutralization. *J. Infect. Dis.* 149:694–702.

Jaffe, J. S., and R. M. Glaeser. 1984. Preparation of frozen-hydrated specimens for high resolution electron microscopy. *Ultramicroscopy.* 13:373–378.

Kalica, A. R., H. B. Greenberg, R. G. Wyatt, J. Flores, M. M. Sereno, A. Z. Kapikian, and R. M. Chanock. 1981. Genes of human (Strain Wa) and bovine (Strain UK) rotaviruses that code for neutralization and subgroup antigens. *Virology.* 112:385–390.

Kalica, A. R., J. Flores, and H. B. Greenberg. 1983. Identification of the rotaviral gene that codes for hemagglutination and protease-enhanced plaque formation. *Virology.* 125:194–205.

Kaljot, K. T., R. D. Shaw, D. H. Rubin, and H. B. Greenberg. 1988. Infectious rotavirus enters cells by direct cell membrane penetration, not by endocytosis. *J. Virol.* 62:1136–1144.

Kapikian, A. Z., and R. M. Chanock. 1985. Rotaviruses. *In* Virology. B. N.

Fields, D. M. Knipe, R. M. Chanock, J. L. Melnick, B. Roizman, and R. E. Shope, editors. Raven Press. New York. 863–906.

Klug, A., and J. T. Finch. 1968. Structure of viruses of the papilloma-polyoma type. IV. Analysis of tilting experiments in the electron microscope. *J. Mol. Biol.* 31:1–12.

Liu, M., P. A. Offit, and M. K. Estes. 1988. Identification of the Simian Rotavirus SA11 Genome Segment 3 Product. *Virology.* 163:26–32.

López, S., C. F. Arias, J. R. Bell, J. H. Strauss, and R. T. Espejo. 1985. Primary structure of the cleavage site associated with trypsin enhancement of rotavirus SA11 infectivity. *Virology.* 144:11–19.

López, S., C. F. Arias, E. Méndez, and R. T. Espejo. 1986. Conservation in rotaviruses of the protein region containing the two sites associated with trypsin enhancement of infectivity. *Virology.* 154:224–227.

Ludert, J. E., F. Gil, F. Liprandi, and J. Esparza. 1986. The structure of the rotavirus inner capsid studied by electron microscopy of chemically disrupted particles. *J. Gen. Virol.* 67:1721–1725.

Mackow, E. R., R. D. Shaw, S. M. Matsui, P. T. Vo, D. A. Benfield, and H. B. Greenberg. 1988a. Characterization of homotypic and heterotypic VP7 neutralization sites of rhesus rotavirus. *Virology.* 165:511–517.

Mackow, E. R., R. D. Shaw, S. M. Matsui, P. T. Vo, M.-N. Dang, and H. B. Greenberg. 1988b. The rhesus rotavirus gene encoding protein VP3: location of amino acids involved in homologous and heterologous rotavirus neutralization and identification of a putative fusion region. *Proc. Natl. Acad. Sci. USA.* 85:645–649.

Martin, M. L., E. L. Palmer, and P. J. Middleton. 1975. Ultrastructure of infantile gastroenteritis virus. *Virology.* 68:146–153.

Midthun, K., H. B. Greenberg, Y. Hoshino, A. Z. Kapikian, R. G. Wyatt, and R. M. Chanock. 1985. Reassortment rotaviruses as potential live rotavirus vaccines candidates. *J. Virol.* 53:949–954.

Milligan, R. A., A. Brisson, and P. N. T. Unwin. 1984. Molecular structure determination of crystalline specimens in frozen aqueous solutions. *Ultramicroscopy.* 13:1–10.

Offit, P. A., G. Blavat, H. B. Greenberg, and H. F. Clark. 1986. Molecular basis of rotavirus virulence: role of gene segment 4. *J. Virol.* 57:46–49.

Offit, P. A., R. D. Shaw, and H. B. Greenberg. 1986. Passive protection against rotavirus-induced diarrhea by monoclonal antibodies to surface proteins vP3 and vP7. *J. Virol.* 58:700–703.

Olson, N. H., and T. S. Baker. 1989. Magnification calibration and the determination of spherical virus diameters using cryo-electron microscopy. *Ultramicroscopy.* 30:281–298.

Palmer, E. L., M. L. Martin, and F. A. Murphy. 1977. Morphology and stability of infantile gastroenteritis virus: comparison with reovirus and bluetongue virus. *J. Gen. Virol.* 35:403–414.

Prasad, B. V. V., G. J. Wang, J. P. M. Clerx, and W. Chiu. 1988. Three-dimensional structure of rotavirus. *J. Mol. Biol.* 199:269–275.

Prasad, B. V. V., J. W. Burns, E. Marietta, M. K. Estes, and W. Chiu. 1990. Localization of VP4 neutralization sites in rotavirus by three-dimensional cryo-electron microscopy. *Nature (Lond.).* 343:476–479.

Roseto, A., J. Escaig, E. Delain, J. Cohen, and R. Scherrer. 1979. Structure of rotaviruses as studied by the freeze-drying technique. *Virology.* 98:471–475.

Sandino, A. M., M. Jashes, G. Faúndez, and E. Spencer. 1986. Role of the inner protein capsid on in vitro human rotavirus transcription. *J. Virol.* 60:797–802.

Shaw, R. D., D. L. Stoner-Ma, M. K. Estes, and H. B. Greenberg. 1985. Specific enzyme-linked immunoassay for rotavirus serotypes 1 and 3. *J. Clin. Microbiol.* 22:286–291.

Taylor, K. A., and R. M. Glaeser. 1976. Electron microscopy of frozen, hydrated biological specimens. *J. Ultrastruct. Res.* 55:448–456.

Unwin, N. 1986. The use of cryoelectron microscopy in elucidating molecular design and mechanisms. *Ann. NY Acad. Sci.* 483:1–4.

Wilson, I. A., J. J. Skehel, and D. C. Wiley. 1981. Structure of the haemagglutinin membrane glycoprotein of influenza virus at 3Å resolution. *Nature (Lond.).* 289:366–373.